The Effectiveness of Time Stretching for Enhancing Dysarthric Speech for Improved Dysarthric Speech Recognition

Prananta, Luke; Halpern, Bence Mark; Feng, Siyuan; Scharenborg, Odette

DOI
10.21437/Interspeech.2022-190

Publication date
2022

Document Version
Final published version

Published in
Proceedings of the Annual Conference of the International Speech Communication Association, INTERSPEECH

Cement and Concrete Research 157 (2022) 106806

Contents lists available at ScienceDirect

Cement and Concrete Research

journal homepage: www.elsevier.com/locate/cemconres

Rheology of alkali-activated slag pastes: New insight from microstructural investigations by cryo-SEM

Yubo Sun [a], Shizhe Zhang [b], A.V. Rahul [a], Yaxin Tao [a], Filip Van Bockstaele [c], Koen Dewettinck [c], Guang Ye [a,b], Geert De Schutter [a,*]

[a] Magnel-Vandepitte Laboratory, Department of Structural Engineering and Building Materials, Ghent University, 9052 Ghent, Belgium
[b] Microlab, Section of Materials and Environment, Faculty of Civil Engineering and Geosciences, Delft University of Technology, Stevinweg 1, 2628 CN Delft, the Netherlands
[c] Laboratory of Food Technology and Engineering, Department of Food Quality and Food Safety, Ghent University, 9000 Ghent, Belgium

ARTICLE INFO

Keywords:
Alkali-activated materials
Blast furnace slag
Rheology
Microstructure
Cryo-SEM

ABSTRACT

This study aims to interpret the early-stage rheology of alkali-activated slag (AAS) paste from microstructure perspectives. The microstructures visualized by cryogenic scanning electron microscopy (cryo-SEM) revealed the essential distinction between hydroxide and silicate-activated slag pastes. The hydroxide-based mixture showed typical suspension features, where slag particles were dispersed in the hydroxide activators. In the hydroxide media, even at very early ages (5 min), the solid grains were attached to each other through rigid connections of reaction products, which resulted in high yield stress. As for the silicate-based mixtures, an emulsion phase has been observed between slag particles, which consists of discontinuous water droplets and continuous silicate gels. Fine emulsions with smaller water droplets were observed as the silicate modulus of activators increased, which dispersed the slag particles but on the other hand improved the viscosity of the paste. With increasing water to binder ratio, both yield stress and viscosity of AAS pastes significantly reduced.

1. Introduction

Production of Portland cement (PC) clinker is a highly energy-consuming process, accompanied by the heavy emission of greenhouse gases. The cement industry has been blamed to be responsible for more than of 5% global CO_2 emissions, which resulted in a great environmental impact [1–3]. Alkali-activated material (AAM) is regarded as a green alternative binding material to replace Portland cement with equivalent and even better mechanical and long-term properties [4–9]. However, the uncontrolled setting process and undesirably poor workability of AAM have been frequently addressed, especially when silicate solution is used as the activator [10–13].

Comparing to PC materials, the alkaline compound is an additional phase in AAM to promote the dissolution of solid particles [14,15]. Its interaction with the solid precursor particles also makes the reactions in AAMs more complex. Starting from each design factor (for instance, the nature of precursors and activators, liquid-to-solid ratio, and admixtures, etc.), the rheological properties of AAMs have been intensively investigated in previous studies [10,13,16–19]. Further, the rheology of AAM mixtures also change dynamically with time, dependent on the real-time packing patterns and interparticle interactions, which are closely correlated to the microstructural arrangement in the fresh mixtures [20]. Therefore, it's crucial to have a fundamental understanding of the relation between rheology and microstructure to optimize the flow of AAM mixtures, which is still missing to date.

The early-stage microstructure characterization of fresh cementitious materials is challenging. Conventional visualization by scanning electron microscopy (SEM) analyses are not applicable for a fresh paste in a hydrous or liquid state [21]. Some innovative in-situ testing methods have been employed (such as ESEM, FBRM/PVM, etc.) to investigate the microstructural features of fresh cementitious mixtures [22–26]. However, such understanding of early-stage AAM mixtures is very limited up to date. Previous studies on the microstructure evolution of AAM pastes have focused more on the solid fraction by using a destructive method. Through a solvent replacement technique, the liquid portion in the fresh paste was replaced with various organic solvents [27–30] to stop the activation process. Afterwards, the solid residues were collected by filtration for visualization through SEM.

* Corresponding author.
E-mail address: Geert.DeSchutter@UGent.be (G. De Schutter).

https://doi.org/10.1016/j.cemconres.2022.106806
Received 26 October 2021; Received in revised form 5 April 2022; Accepted 6 April 2022
Available online 13 April 2022

However, it should be noted that the pore solution previously distributed between solid voids as the solvent is removed through the extraction, while the solid particles which were originally floating in the pore solutions are deposited as compacted sediment [31]. As a result, the primal spatial arrangement in the fresh AAM paste cannot be visualized by this technique. Furthermore, the solvent replacement normally has to be performed several times until the original pore solution can be completely substituted. This makes it difficult to accurately terminate the activation process at a specific time in the early stage for microstructural characterization.

The development of cryogenic SEM (cryo-SEM), which includes a sublimation step, has enabled the visualization of hydrating and high-moist samples. Liquid, beam, and vacuum sensitive specimens can be set into a steady-state through cryogenic preparation [21], as has been broadly applied in biological and material science engineering [32–36]. Moreover, the artificial rearrangement of the microstructure induced by ice crystallization [21,37–39] during cryo-SEM imaging can be prevented through an ultrarapid freezing process [37,40–43], and thus the nature of microstructures is well preserved [31].

The objective of this study is to better understand the rheological behavior of fresh alkali-activated slag (AAS) paste from microstructural perspectives. The structural build-up of AAS paste was characterized by the storage modulus and loss factor evolution determined by small amplitude oscillation shear (SAOS) test, while the rheological parameters were derived from stress growth and flow curve tests. The microstructural features of AAS mixtures at very early ages were visualized by cryo-SEM. A quantitative analysis was provided to explore the microstructural evolution of AAS pastes by varying the key design factors (including the composition of activators, silicate modulus, and water to binder ratio), which brings new insight into the early-stage rheological behavior.

2. Materials and methods

2.1. Materials

The blast furnace slag (BFS) used in this study was provided by Ecocem Benelux B.V., with a density of 2890 kg/m^3. The particle size distribution measured by laser diffraction is shown in Fig. 1(a), (d_{50} = 8.28 μm). Morphology of BFS particles was observed with a scanning electron microscope (SEM), as shown in Fig. 1(b). Details of the chemical composition of BFS determined by X-ray fluorescence (XRF) and loss on ignition (LOI) are listed in Table 1.

In this study, blank mixtures where no alkali-activation takes place have been designed to study the interactions between precursors and activators by using cryo-SEM. It's been reported that quartz sand, which mainly consists of crystalline phases, has a relatively low alkali-susceptibility/reactivity [44]. Micronized quartz sand (d_{50} = 26.67 μm) produced by grinding of quartz sand was selected as an "inert" precursor. A reference mixture was prepared with quartz sand and the activator to study the effect of sodium silicate on the early-stage microstructural arrangement. The chemical composition of quartz sand is given in Table 1.

Sodium hydroxide and sodium silicate solution, the most commonly used alkaline activators in AAM, were applied in this study. Reagent-grade sodium hydroxide anhydrous pearls were provided by Brenntag N.V., and the sodium silicate solution (15% Na_2O, 30% SiO_2, and 55% water) was provided by PQ Corporation.

In previous studies, organic solvents [27–30] have been applied as the reaction termination media to stop the alkali-activation process. The organic solvent 2-propanol was applied as an "inert" activator to study the early-stage microstructural arrangement features.

2.2. Mixture proportions

Details of AAS paste mixtures tested in this study are presented in Table 2. In all AAS mixtures, the sodium concentration (Na_2O to BFS mass ratio) was kept constant at 4% [45]. The alkaline activator for each AAS mixture was prepared by dissolving alkaline compounds into tap water one day before mixing. The effects of activator solution, silicate modulus (Ms), and water to binder ratio (w/b) were investigated by varying design factors.

M1 and M3 were designed as the reference AAS paste activated by sodium hydroxide and sodium silicate solutions, respectively. The interaction between solid and liquid phases in AAS pastes was studied by using different combinations of alkaline activators and precursors in M1, M3, M9, and M10. M9 and M10 were designed as blank mixtures, where the activator and precursors were replaced with the "inert" materials, respectively. M2 to M6 were designed to study the effect of silicate concentration in the activator, by varying the Ms. from 0.125 to 2.0. In the meantime, M7 and M8 were designed to evaluate the effect of water content with elevated w/b.

2.3. Experimental method

2.3.1. Mixing procedure

The fresh AAS paste mixtures used for the rheological tests in this study were prepared with a Hobart planetary mixer. The solid precursor was first added into the mixer bowl and dry-blended at 140 ± 5 rpm for 60 s. Afterwards, the activator solution was gradually added to the mixer within 10 s. The precursor and activator were mixed at low (140 ± 5 rpm) and high (285 ± 5 rpm) speeds for 90 s, respectively. The entire mixing procedure was finished in 180 s ever since the wetting of precursors, and the fresh AAS mixture was used for subsequent rheological tests.

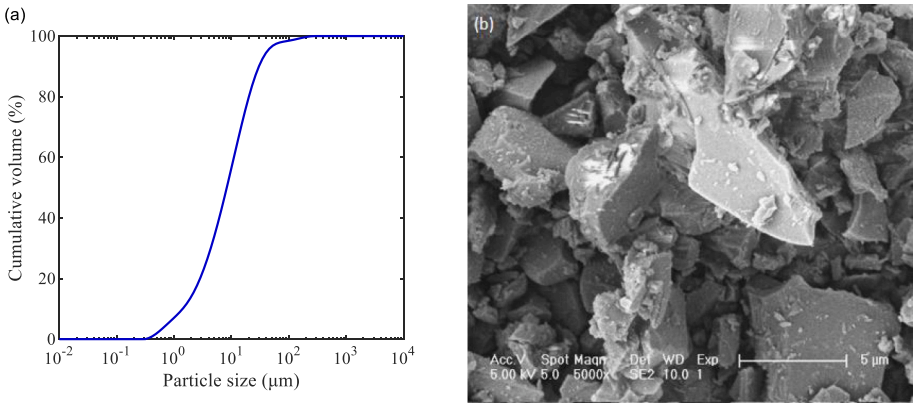

Fig. 1. Physical properties of BFS (a) Particle size distribution; (b) Morphology by SEM (5000×magnification).

Table 1
Chemical composition of BFS measured by XRF and LOI (mass %).

Precursor	CaO	SiO_2	Al_2O_3	MgO	SO_3	TiO_2	K_2O	Fe_2O_3	MnO	ZrO_2	Other	LOI[a]
BFS	40.9	31.1	13.7	9.16	2.31	1.26	0.69	0.40	0.31	0.12	0.05	0.10
Quartz sand	0.25	97.3	0.37	0.34	0.02	0.03	0.26	0.89	0.17	0.05	0.32	0.17

[a] LOI measured by thermogravimetric analysis at 950 °C.

Table 2
Mixture proportion of AAS pastes.

Mix	BFS[a] (g)	Activator (g)		Na_2O[b]	Ms[c]	Admixture[b]	w/b[d]	Water (g)
		Sodium hydroxide	Sodium silicate					
M1	100	5.16	0	4%	0	0	0.4	42.06
M2	100	4.84	1.67	4%	0.125	0	0.4	41.32
M3	100	3.87	6.67	4%	0.5	0	0.4	39.08
M4	100	2.58	13.33	4%	1	0	0.4	36.10
M5	100	1.29	20.00	4%	1.5	0	0.4	33.12
M6	100	0	22.67	4%	2	0	0.4	30.13
M7	100	3.87	6.67	4%	0.5	0	0.45	44.72
M8	100	3.87	6.67	4%	0.5	0	0.5	49.77
M9	100	0	0	0	0	0	0.4	2-propanol, 40[e]
M10	Quartz sand, 100[f]	3.87	6.67	4%	0.5	0	0.4	39.09

[a] The mass of precursor was fixed at 100 g for each mixture in this study.
[b] Represented as the mass percentage of precursor.
[c] Defined as the molar ratio between SiO_2 and Na_2O in activators.
[d] Defined as water content in both aqueous activator and water added separately from the activator divided by the sum of precursor and solid activators.
[e] In M9, all liquid components were replaced with the "inert" activator 2-propanol.
[f] In M10, BFS was replaced with the "inert" precursor micronized quartz sand.

2.3.2. Rheological tests

The rheological properties of AAS pastes were measured with Anton Paar MCR 102 rheometer fitted with a 6-blade vane having 22 mm diameter, and 16 mm height. For each test, a new AAS paste was prepared to avoid the effect of shear history from previous measurements. The fresh AAS paste was loaded into a cylindrical cup (27.6 mm inner diameter and 75 mm depth). The temperature was controlled at 20 ± 0.5 °C with a water bath system during each measurement.

The structural build-up of AAS paste was assessed by a small amplitude oscillation shear (SAOS) test. First, a strain-sweep with the strain amplitude varying from 0.0001% to 10% with a constant frequency of 1 Hz [17,46,47] was conducted to determine the linear viscoelastic domain (LVED). Subsequently, a time-sweep was performed at a constant frequency of 1 Hz and at a constant strain amplitude of 0.005% (within the LVED) from 8 min after the wetting of precursors to 60 min to assess the structural build-up with respect to time. Similar approaches have also been used by other researchers to characterize the structural build-up of cementitious systems [17,48,49]. The viscoelastic behavior of AAS pastes can be described by the storage modulus (G′) and loss modulus (G″) [49], which represents the energy stored and dissipated in the mixture in each cycle of excitation, respectively. In this study, the storage modulus and loss factor (the ratio between G′ and G″, which indicates the phase lag between the elastic and viscous portions) were presented to characterize the structural build-up of AAS pastes. For each AAS mixture, the SAOS test was performed on 3 replicate samples to ensure repeatability, and the curve most close to the average of 3 measurements is presented.

The static yield stress of AAS paste was determined by the stress growth test. AAS paste in the rheometer cup was first subjected to a 150 s^{-1} pre-shear for 30 s ensuring all samples reached an identical reference state [46,50]. The paste was then subjected to a rest duration of 30 s to release the residual stress [46,51]. Following this, a constant shear rate of 0.1 s^{-1} was applied for 60 s [52]. By applying a constant shear rate, the shear stress first increased to the maximum, and then progressively decreased to finally reach a steady state value [53]. The static yield stress is expressed as the maximum shear stress that is reached during the stress growth test. Stress growth tests were conducted at 6 min after the wetting of precursors.

As shown in Fig. 2, the flow curve test was also conducted to determine the dynamic yield stress and plastic viscosity. A 150 s^{-1} pre-shear was applied for 30 s, and the fresh AAS paste was left at rest for another 30 s until the flow curve test. This is followed by an increase in shear rate in steps of 25 s^{-1} with each step lasting for 1 min and to reach a maximum shear rate of 150 s^{-1}. Afterwards, the shear rate was ramped down from 150 s^{-1} to 25 s^{-1}. The dynamic yield stress and plastic viscosity were determined by fitting the ramp down portion of the flow curve with the Bingham model [18,19]. In addition, the hysteresis loop curve area was calculated to assess the thixotropic behavior in AAS pastes [54,55]. For each mixture, the test was repeated 3 times, and the averaged rheological parameters are presented.

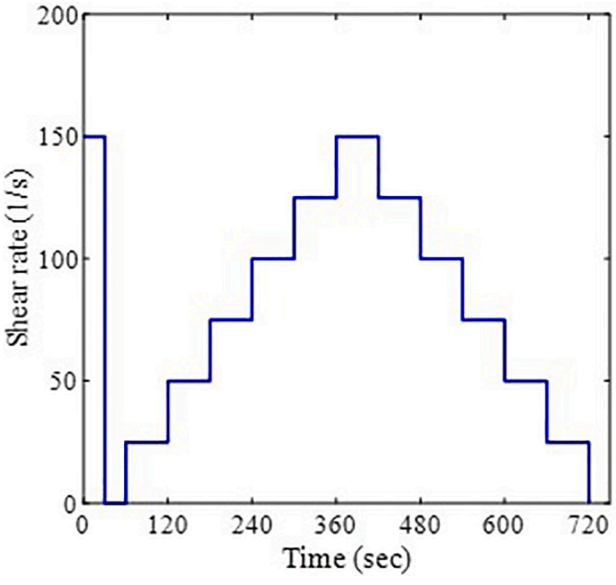

Fig. 2. Shear protocol applied in flow curve tests.

2.3.3. Microstructural investigation

The microstructure of fresh AAS paste was investigated by cryo-SEM, using a JSM-7100F TTLS LV TFEG-SEM (JEOL Ltd., Tokyo, Japan). AAS pastes for cryo-SEM investigation was prepared by mixing precursors and activator solutions. The mixture was subjected to a 2-min strong manual mixing and left at rest until the target testing ages. In addition, a manual remix of 30 s followed by a rest duration of 30 s was applied to the sample before the cryo-SEM experiment. The fresh paste sample at 5 min after wetting was first vitrified in a nitrogen slush (−210 °C, which can effectively prevent the ice crystallization [40–43]) to suspend the activation reaction. Afterwards, the vitrified sample was immediately transferred under vacuum conditions into PP3010T cryo-SEM preparation system (Quorum Technologies Ltd., East Sussex, U.K.) conditioned at −140 °C. Subsequently, the sample was fractured with a cooled knife and subjected to a 1-hour etching process at −90 °C in the preparation chamber to sublimate the water content. A thin layer of conductive metal (Pt) was sputter-coated on the surface of AAS samples using argon gas to prevent charging during electron beam targeting [56]. SEM observation was performed at −140 °C under vacuum conditions ($1e^{-6}$ mbar) and at an accelerated voltage of 3 kV. For each mixture, ten pictures were captured from random positions for image analysis. Moreover, the cryo-SEM observation was performed on M3 at 20 and 60 min as well to study the microstructural evolution of silicate-based mixtures along the activation process (Note: only 3 images were captured from M3 at 60 min since it was too stiff to create more fracture surface under the frozen state for visualization). The cryo-SEM images were taken under 1000 and 5000×magnifications (0.093 and 0.019 μm resolution, respectively), and the image analysis were performed under 1000×magnification on a frame size of 1280×1024 pixels.

A porous gel-like network structure was detected in AAS pastes made of silicate-based activators (see Fig. 3), and it was found that the pore size varies by changing the design factors. Image analysis was performed on the micrographs obtained from cryo-SEM using the ImageJ software [57] to characterize the properties of pores. To be specific, the cryo-SEM images were first converted into an 8-bit greyscale image. The grayscale image was subsequently binarized to separate the solid grains and network structure from the liquid phase. As shown in Fig. 3, the network structure is indicated by the red square, and the big solid grain in the blue square is representative for slag particles. Afterwards, the area of each pore was determined by the software. Starting from the smallest pore detected in each mixture, the area of pores was summed up to derive a cumulative pore area distribution (from 0% to 100%). Furthermore, A_{50} was defined as the average pore area in each image when the cumulative percentage reaches 50%.

3. Results and discussion

3.1. Rheology of AAS pastes

3.1.1. Critical strain of AAS paste

The strain-sweep was first conducted to determine the LVED, the evolution curves of oscillation stress are presented in Fig. 4. In the majority of AAS mixtures, linear growth in a double logarithmic plot was detected in the low strain amplitude region. Peak stress occurred at around 0.1%, followed by a gradual reduction in stress with further increases in the strain amplitude. Similar results have been reported by Beersaerts et al. [58]. It is noteworthy that the greatest peak stress was detected in M3 with a silicate modulus of 0.125, which is even higher than the hydroxide mixture M1. The stress evolution was progressively declined with a further increase in Ms. (from 0.5 to 1.5), while the peak located at around 0.1% became less significant as well. Alnahhal et al. [46] observed a small peak of stress at a strain value at around 0.03% in a BFS-FA blended mixture, which was correlated to the formation of primary C-A-S-H gels in a Ca-rich system [27,59]. However, a higher stress level was achieved in M6 (Ms2.0) as compared to M5 (Ms1.5), which can be attributed to the presence of colloidal silicate complexes in a highly concentrated silicate solution [18,58], and thus contributed to higher stress in the AAS mixture. Meanwhile, as presented in Fig. 4(b), the extra water content led to the reduction in oscillation stress along with the strain amplitude.

The G′ responses of different AAS pastes over the strain-sweep are shown in Fig. 5. An initial plateau has been observed at relatively low strain ranges among all mixtures, followed by a reduction in G′ under higher strain amplitude. The strain beyond which G′ decreased is considered as the critical strain [47], and the structuration is broken down as the shear excitation applied exceeded the strain capacity of the AAS paste. As presented in Fig. 5, the critical strain of all AAS pastes ranged between 0.01% and 0.1%, regardless of the Ms. and w/b ratio. Thus, the subsequent time-sweep was performed with a strain amplitude of 0.005% within the LVED.

3.1.2. Viscoelastic behavior of AAS pastes

The G′ evolution as a function of time in different AAS pastes is presented in Fig. 6. As shown in Fig. 6(a), almost linear growth in the G′ has been detected in M1, where no silicate was present in the activator. In a hydroxide-based AAS mixture, the majority of elemental components are completely dissolved from the precursors to form the polymerization product (C-A-S-H gels), while the activator solutions provide elevated alkalinity to promote the dissolution. It is indicated that the structural build-up in M1 can be ascribed to the precipitation of reaction products around individual slag grains [17], which progressively bridged the precursor particles to form a percolation network [60].

On the other hand, the silicate-based AAS mixtures exhibited different G′ development features by varying Ms. in the activator. In the

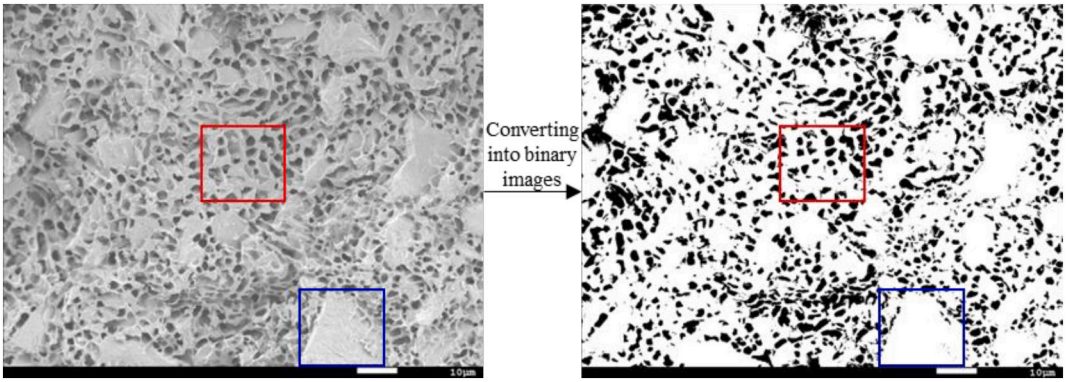

Fig. 3. Cryo-SEM image analysis protocol.

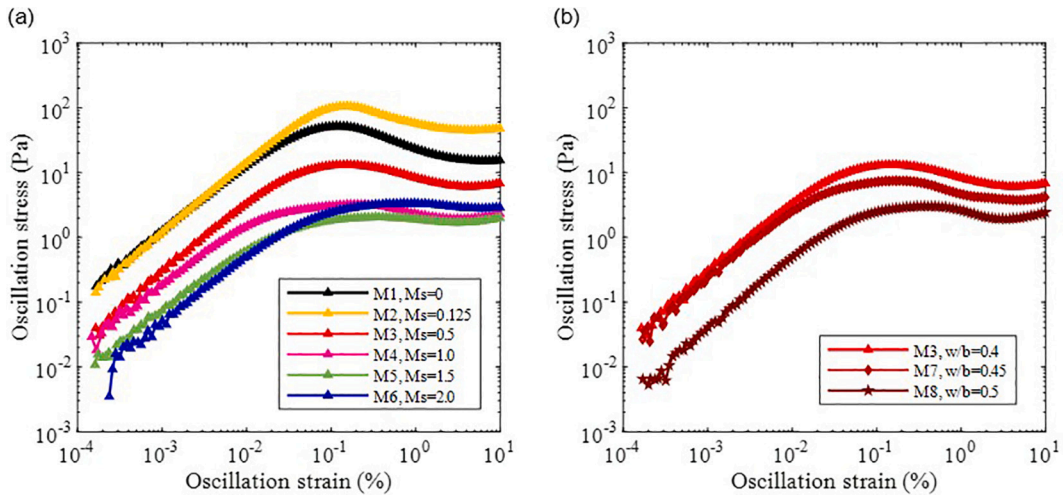

Fig. 4. Evolution of oscillation stress as a function of strain (a) Effect of Ms.; (b) Effect of w/b ratio.

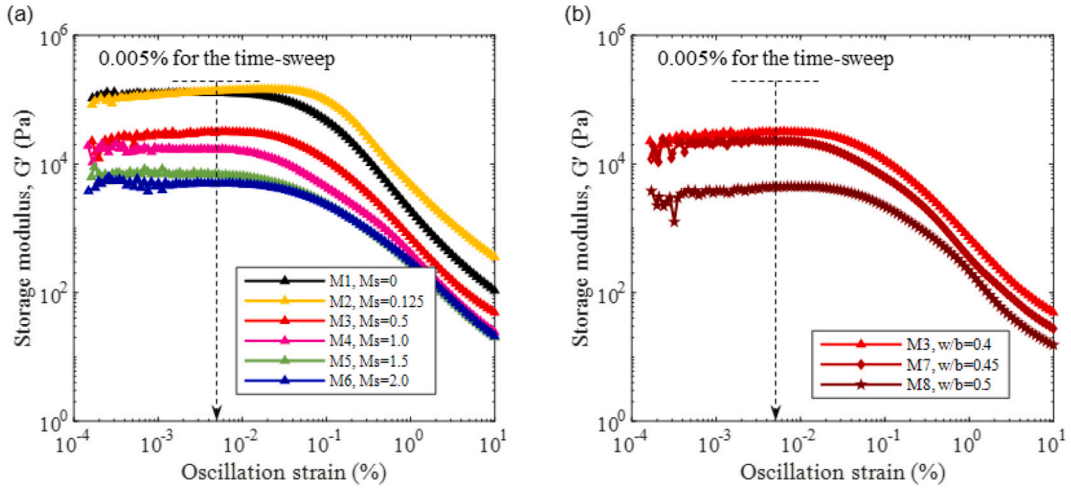

Fig. 5. Evolution of storage modulus as a function of strain (a) Effect of Ms.; (b) Effect of w/b ratio.

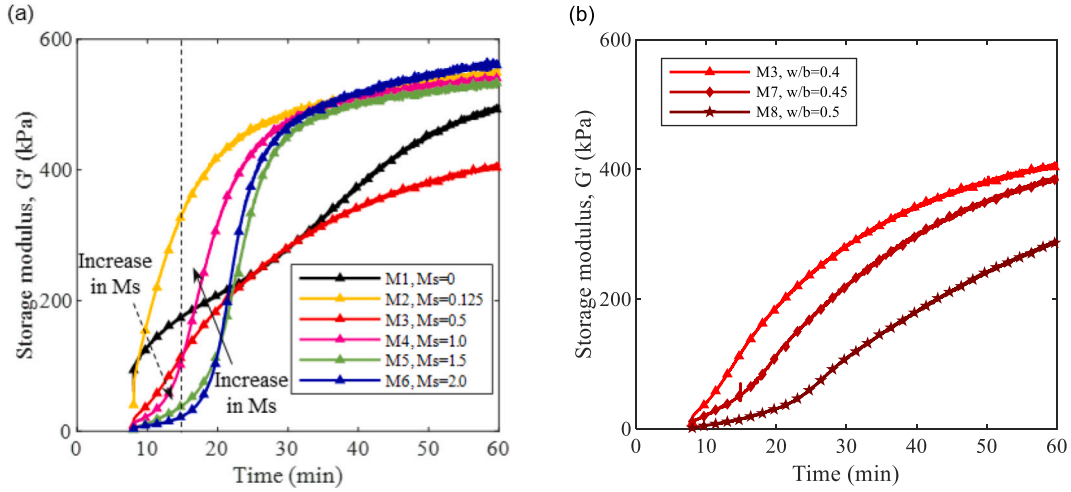

Fig. 6. Evolution of storage modulus as a function of time (a) Effect of Ms.; (b) Effect of w/b ratio.

case of a low Ms. mixture, the G′ of M2 (Ms0.125) developed sharply at the first couple of minutes and quickly reached a relatively stable high level after 30 min, which reveals the fast formation of a well-percolated network structure [61]. A trace amount of silicate species in M2 provided extra nucleation sites in the pore solution to facilitate the reaction process [62]. The precipitation of reaction products takes place

simultaneously in both pore solution and on the slag surface, which leads to a more rapid structural build-up as compared to the hydroxide-based mixture M1. With a further increase in Ms., as indicated by the dashed arrow in Fig. 6(a), the very early-stage structuration of AAS pastes approximately before 15 min was gradually attenuated. Almost no significant increase in G′ has been observed in M5 and M6 at this stage, which reveals that the structural formation is very limited indicating a dormant period. The slow early structural build-up can be attributed to the extra silicates applied in the activator, which not only reduced the alkalinity in the pore solution to slow down the dissolution [12] but also increased the liquid content in the AAS mixture and resulted in less elastic behavior. However, this dormant period is distinctive from the induction period detected by the calorimetry studies in AAS mixtures with a high Ms., which can last from hours to days [63,64]. The lowest G′ has been observed in M3 after 60 min, accompanied with a slight reduction in the slope of G′ evolution after about 30 min. This can be explained by the limited ion diffusion rate along the reaction process. A reaction ring on the slag surface has been reported by previous studies [17,62], which can be interpreted as a Si-rich layer formed due to the dissolution of other elements along the reaction process [60,65]. Apart from that, the early reaction products also wrapped around the outer surface to slow down the dissolution of unreacted slag particles [66]. Accordingly, both the inner and outer reaction products [62] obstructed the ion exchange between the activator solution and unreacted slag particles and thereby decelerated the structural build-up in M3. Moreover, a very steep increase in G′ occurred in M4, M5, and M6 after the initial dormant period. It's been observed that the higher the Ms., the greater the structural build-up rate at this stage as indicated by the solid arrow in Fig. 6(a). Palacios et al. [27] also reported a similar fast increase of the storage modulus in an Ms1.5 AAS mixture, and the rapid loss in workability can be attributed to the accumulation of primary C-(A)-S-H gels, which is the intermediate reaction products between the Ca, Al dissolved from slag particles and the silicate species in the activator [10,67].

With an increased w/b ratio, the structural build-up of AAS paste is gradually slowed down as shown in Fig. 6(b). The higher water content resulted in lower alkalinity in the activator, which slowed down the dissolution of precursors and thus result in slower structural development. In addition, a more porous AAS microstructure is formed due to the extra water content. In that case, more reaction products and longer time are needed to establish a rigid network.

The loss factor evolution of AAS paste is presented in Fig. 7, showing the effects of Ms. and w/b ratio. A rapid reduction in the loss factor has been observed in M1 and M2 (Fig. 7(a)) at the first several minutes, in line with the fast structural build-up in these mixtures. The loss factor of M2 reached 0 at around 20 min, indicating a pure elastic behavior in the mixture as well as the formation of a percolated network [68]. With the increase in Ms., higher initial loss factors have been detected, which reveals a more viscous behavior in the AAS mixtures due to the extra liquid silicate content. It is noteworthy that a hump occurred on the loss factor curves in M5 and M6 as the reaction progressed (indicated by the arrow in Fig. 7(a)), which reveals a partial dissipation of the stored energy at the beginning of polymerization [69]. Previous studies suggested this can be correlated to the free water released due to the polycondensation [70,71], contributing to the viscous behavior over the elastic portion. On the other hand, the loss factor over time was significantly increased with an elevated w/b ratio, as shown in Fig. 7(b). The addition of extra water content enhanced the viscous behavior of AAS paste at the beginning, and also extended the time required to reach an elastic state.

3.1.3. Flow curves of AAS pastes

Flow curves of AAS paste with different Ms. and w/b ratios are shown in Fig. 8, and hysteresis loops have been observed in all mixtures. The rheological parameters of AAS pastes are summarized in Table 3. A gradual reduction in dynamic yield stress from 144.39 Pa to 7.10 Pa has been detected when the Ms. was increased from 0 to 2.0, confirming the fluidizing effect of sodium silicate solutions [19]. In the meantime, the plastic viscosity was reduced by 16.7% in M3 comparing to M1, while further increase in Ms. resulted in the higher viscosity of M4, M5, and M6, which was around 2.5 Pa·s in these mixtures. The degree of thixotropy in AAS mixtures was reflected by the area between up and down ramp flow curves. By varying the Ms., the greatest loop curve area was detected in M2 (Ms0.125), which is in agreement with the G′ evolution detected by the SAOS test. A more flocculated structure can be expected due to the rapid initial structural build-up, which also resulted in the highest static yield stress in M2. However, this initial structuration is reversible such that the dynamic yield stress of M2 is 26.7% lower as compared to M1. Regarding the effect of water content, an increase in the w/b ratio resulted in significant reductions in all rheological parameters listed in Table 3. It is indicated that the solid precursor grains are more dispersed by the extra water content [72].

3.2. Microstructural features of AAS pastes

3.2.1. Effect of activators

Microstructures of M1, M3, M9, and M10 at 5 min are presented in Fig. 9. Firstly, Fig. 9(a) and (c) show the micrograph obtained when hydroxide and 2-propanol media are used, respectively. As shown in Fig. 9(c), irregular-shaped angular BFS particles have been observed,

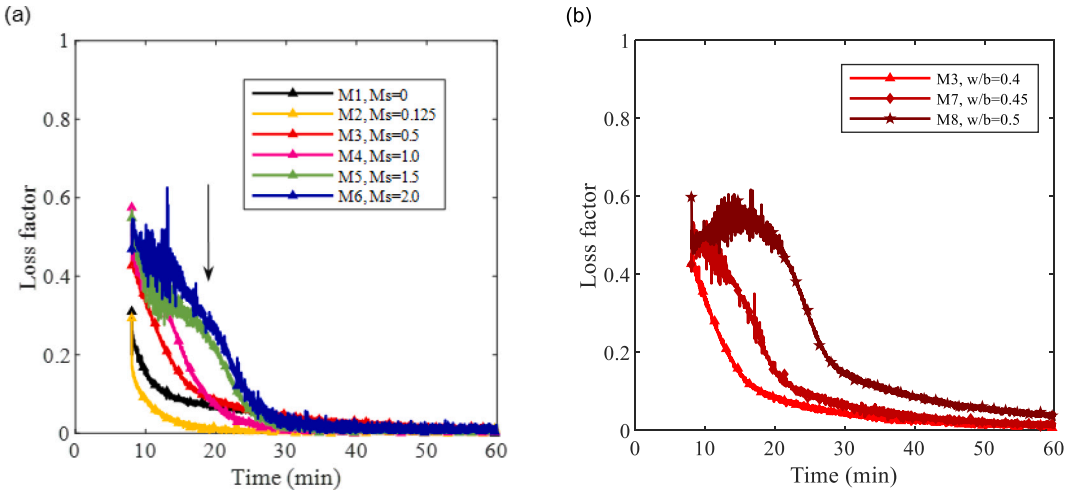

Fig. 7. Evolution of loss factor as a function of time (a) Effect of Ms.; (b) Effect of w/b ratio.

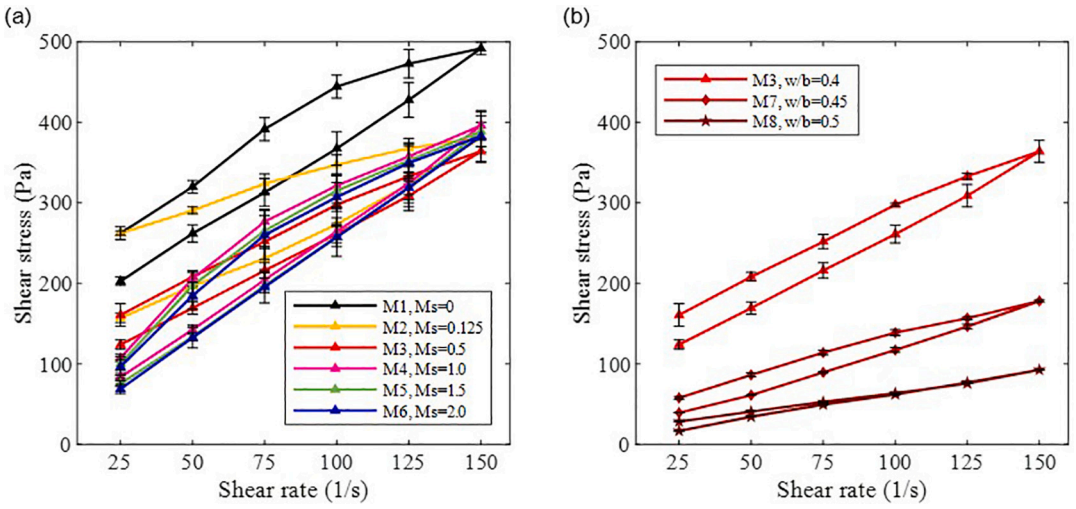

Fig. 8. Flow curves of AAS pastes (a) Effect of Ms.; (b) Effect of w/b ratio.

Table 3
Rheological parameters of AAS pastes.

Mix	Static yield stress (Pa)	Dynamic rheological parameters (fitted with Bingham model)			Loop curve area (Pa/s)
		Dynamic yield stress (Pa)	Plastic viscosity (Pa·s)	R^2	
M1	275.31	144.39	2.28	0.9987	7207.44
M2	326.28	105.91	1.77	0.9909	8945.77
M3	169.31	74.33	1.90	0.9988	3838.88
M4	64.89	19.30	2.48	0.9990	5945.76
M5	45.36	10.52	2.49	0.9994	5861.83
M6	34.29	7.10	2.51	0.9999	5271.86
M7	22.38	7.75	1.12	0.9973	2269.51
M8	11.19	3.54	0.59	0.9982	393.65

which was very similar to the original morphology of BFS (Fig. 1(b)). Agglomeration of slag particles was observed where smaller particles were closely attached to the surface of large grains. The interparticle cavities represent the space originally occupied by water, which was sublimated during the etching process. When sodium hydroxide activator is used, a thin layer of amorphous reaction products was observed on the particle surface (see Fig. 9(a)). This indicates that the reaction proceeded very rapidly in sodium hydroxide media such that the reaction products already precipitated on the BFS surface at 5 min after wetting. In both 2-propanol and sodium hydroxide media, a clear boundary adjacent to the surface of slag particles could be identified as the water content was sublimated.

However, significant changes in the microstructural features of interparticle phases occurred as the sodium silicate was applied. As shown in Fig. 9(b), a porous network structure appeared between slag particles. The network structure consists of gel-like skeletons and semi-connected pores (some pores are connected to each other through openings on inner walls), which were formed due to the sublimation of water droplets. Further, it can be observed that the slag particles were tightly wrapped up and bridged to each other through the network structures. A similar microstructure was observed in Fig. 9(d) (M10, made of silicate-based activator and the "inert" precursor) as well, where no dissolution or activation reaction takes place. Therefore, the presence of the gel-like network structure detected in M10 is attributed to the activator phase. Moreover, almost identical microstructures have been observed in Fig. 9(b) and (d), while the network structure wrapping around slag particles was not observed in hydroxide-based mixtures (Fig. 9(a)). It is indicated that the network structure is formed due to the presence of sodium silicate. A schematic microstructure sketch of AAS paste is illustrated in Fig. 10, which will be further explained to interpret the rheological parameters.

Dai et al. [17] studied the pore solution chemistry of a similar AAM mixture (Ms0.4) made of BFS and fly ash, and they reported that the pore solution was dominant by Na and Si at 10 min after wetting, while only very limited quantities of Al and Ca dissolved from precursors were identified. The result further illustrates that the network structure is formed due to the activator. The tiny reduction in Si concentrations might be indicative of the formation of N-A-S-H precursor gel and C-(N)-A-S-H [27] at the very early stage of the activation reaction. Previous studies suggested that the silicate content in activators can provide nucleation sites for the reaction products [62,73]. However, no obvious changes in microstructural features in cryo-SEM images have been detected, and the reaction products are scarcely observed on the silicate gel network. It might be ascribed to that the pore solution did not reach the supersaturation to form the precipitations [27], or the low amount of reaction products can be buried in the silicate gels.

Meanwhile, Favier et al. [74] studied the colloidal interactions between metakaolin grains when suspended in a silicate-based alkaline solution. It was observed that the colloidal interactions between the precursor grains are of very low energy, which results in a suspension with very low yield stress. On the other hand, the hydrodynamic viscous dissipation was found to be a predominant mechanism in the silicate media, resulting in a high macroscopic viscosity of the suspension. Besides, Kashani et al. [75] reported a transition from negative to positive zeta potential value in a hydroxide-based AAS mixture with an increased alkali concentration, due to the adsorption of cations on slag surfaces. Conversely, the addition of sodium silicate resulted in greater negative zeta potential values in silicate-based AAS mixtures, which reveals that the slag particles are wrapped around by the negatively charged silicate species [66]. Moreover, they also detected attractive double layer forces in mixtures with a high silicate dosage, which can be linked to the bridging of slag particles through the network structures, as shown in Fig. 9(b).

Comparing Fig. 9(a) and (b), it can be observed that the AAM in hydroxide media showed a suspension type behavior (solid particles dispersed in a liquid media) [76] whereas in the presence of silicates, the pore solution phase between slag particles showed typical emulsion characteristics, where two liquid phases immiscible to each other formed a dispersion of liquid droplets in a continuous liquid medium [77,78]. In that case, the AAS paste prepared using silicate-based activators could be interpreted as a complex multi-phasic dispersion, where BFS particles are dissolved in a "water-in-silicate" emulsion.

Regarding the rheological parameters, both static and dynamic yield stress in M1 were drastically declined (by 38.5% and 42.5%,

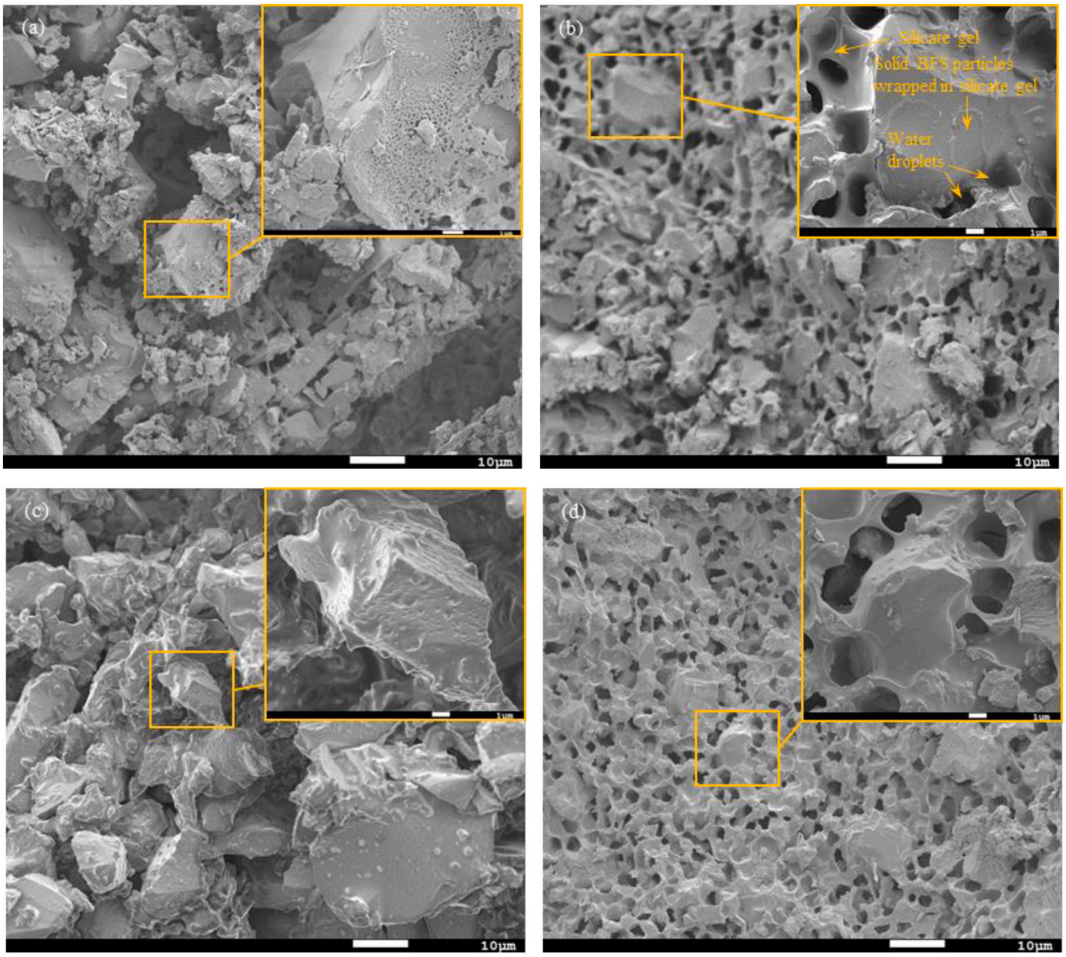

Fig. 9. Microstructure of fresh paste by cryo-SEM (1000 and 5000×magnification) at 5 min. (a) M1, BFS with hydroxide-based activator; (b) M3, BFS with silicate-based activator (Ms0.5); (c) M9, BFS with 2-propanol; (d) M10, quartz sand with silicate-based activator (Ms0.5).

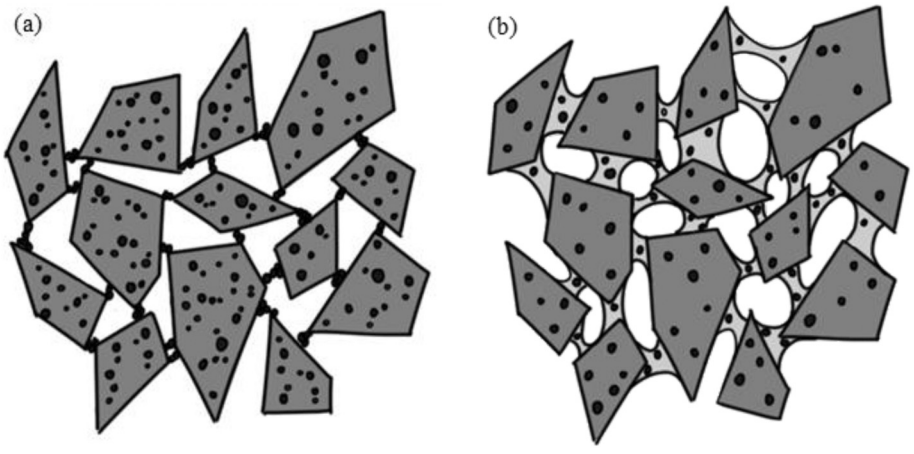

Fig. 10. Schematic diagram of microstructures (a) Hydroxide-based AAS paste; (b) Silicate-based AAS paste.

respectively) with the involvement of the silicate content in the activator, which confirmed the fluidizing effect of sodium silicate [19]. Meanwhile, the plastic viscosity of M3 also reduced by 16.7% as compared to M1. The high yield stress of AAM in the hydroxide media compared to the silicate media can be explained based on the microstructures visualized in Fig. 9. As discussed earlier, the hydroxide media showed a suspension-like behavior, i.e., the slag particles are dissolved in the hydroxide solution to form a suspension, which is consistent with PC mixtures [76]. However, as the solid reaction products progressively precipitate on the surface particles as the reaction proceeds and the slag particles are bridged to each other due to the accumulation of reaction products. This is schematically shown in Fig. 10. Further, the agglomerations of the slag particles cause the free water to be trapped in flocs [16,79]. Externally applied shear has to break the agglomeration between solid slag particles and reaction products to initiate the flow, which leads to the high yield stress detected in hydroxide-based AAS

mixtures. With the presence of silicate in the activator, the system becomes rather complex. According to cryo-SEM observations, a discontinuous bi-phasic liquid occurs between the slag particles as shown in Fig. 10(b), identified as an emulsion consisting of the continuous silicate gel and water droplets. Compared to the more rigid connections formed by the reaction products in the hydroxide media (Fig. 10(a)), the bi-phasic liquid structure in the silicate media can be broken relatively more easily when subjected to shear [76]. Therefore, the flow initiates more easily in the latter case in a more dispersed mixture, leading to lower yield stress and viscosity as seen in the rheological parameters.

3.2.2. *Effect of Ms*

At a fixed alkali concentration, an increased silicate concentration from Ms0.125 to Ms2.0 was designed in this study to investigate the microstructural features in AAS pastes with different Ms. (M2-M6) at 5 min, and the results are illustrated in Fig. 11. It's been observed that the pore size of water droplets significantly reduced as the Ms. increased. The pore size distribution and A_{50} values are presented in Fig. 12. The results showed that the micropores in area fraction 0.1 to 10 μm^2 remarkably increased in AAS pastes with higher Ms.

As shown in Table 3, both static and dynamic yield stresses of AAS pastes was dramatically reduced as the silicate became more concentrated. Considering the extreme condition in hydroxide-based AAS paste, where no silicate was applied, high yield stress was detected to initiate the flow. However, a network structure was formed with the addition of sodium silicate, which wrapped around the slag particles and resulted in the dispersion of slag particles in the mixture. Direct contacts between solid particles were extensively prevented. This can be correlated to the reduction in dynamic rheological parameters in M2 as compared to M1 (the dynamic yield stress and plastic viscosity were reduced by 26.7% and 22.4%, respectively) when only a small dosage of silicate was applied in the activator. On the other hand, M2 showed a higher static yield stress than M1. This can be interpreted by the rapid structural build-up at the first couple of minutes and the strong thixotropic behavior in M2 (Fig. 6(a) and Table 3). However, as aforementioned, the early-stage reaction products can be buried in the interstitial silicate gels and were not observed by the cryo-SEM images. With further increase in Ms., the fluidizing effect became less significant. For instance, the dynamic yield stress of Ms2.0 mixture only reduced 3.42 Pa compared to Ms1.5 mixture. It is indicated that the direct contact and colloidal interactions progressively reduced, and the solid particles were dispersed sufficiently far apart from each other as more silicate gels appeared in the pore solution [76].

Meanwhile, the plastic viscosity of AAS pastes exhibited a nonlinear variation with the increase in Ms. At low Ms. ranges, the plastic viscosity first improved when Ms. was increased from 0.125 to 1.0, while it almost kept unchanged by further improving the silicate modulus. Once the flow is initiated, the resistance to the flow determines the plastic viscosity. It has been reported in suspensions that the viscosity is directly proportional to the viscosity of the liquid phase and the solid concentration. For instance, the Krieger-Dougherty equation [80,81] expresses the viscosity of suspension as $\eta = \eta_L f\left(\frac{\phi}{\phi_m}\right)$ where η_L is the viscosity of the liquid phase and $f\left(\frac{\phi}{\phi_m}\right)$ is a function of solid volume fraction (ϕ) and maximum possible solid volume fraction (ϕ_m). Alnahhal et al. [46] studied the rheology of activator solutions in AAM with various silicate concentrations, and they found out the viscosity was doubled when Ms. was increased from 1.0 to 1.5. This can be attributed to the nature of emulsions that the fine droplets result in the high viscosity of the mixture [77,82,83]. Microstructural features illustrated in Fig. 11 confirmed the presence of smaller droplets with an increase in Ms., which indicates the viscosity of the activator was increased. However, excess silicate content as the extra liquid phase on the other hand reduced the solid concentration. Accordingly, the plastic viscosity slightly increased as Ms. was increased from 0.125 to 1.0, while afterwards remained almost unchanged with further increasing the silicate concentration.

The above results showed the dispersing effect of silicate content. However, such effect might disappear as the reaction proceeds. Due to the continuous accumulation of reaction products, the silicate network gradually hardens until the mixture loses its fluidity. Previous studies also suggested the hardening process might take place very fast in mixtures with a high Ms. [17,84], referring to the steep increase of G′ after the initial dormant period detected by SAOS test. Therefore, it is possible to improve the initial workability of AAS by using more silicate in the activator, while the fast setting process should be properly controlled in the case of high Ms., this will be further discussed in Section 3.3.

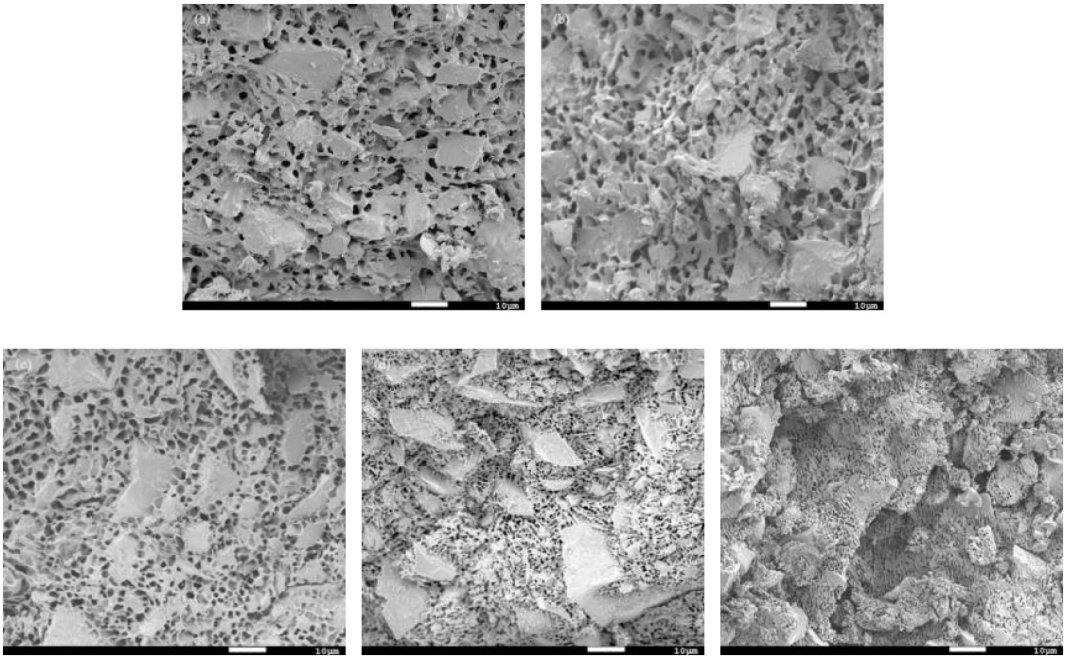

Fig. 11. Microstructure of fresh paste by cryo-SEM (1000×magnification) at 5 min (a) M2, Ms0.125; (b) M3, Ms0.5; (c) M4, Ms1.0; (d) M5, Ms1.5; (e) M6, Ms2.0.

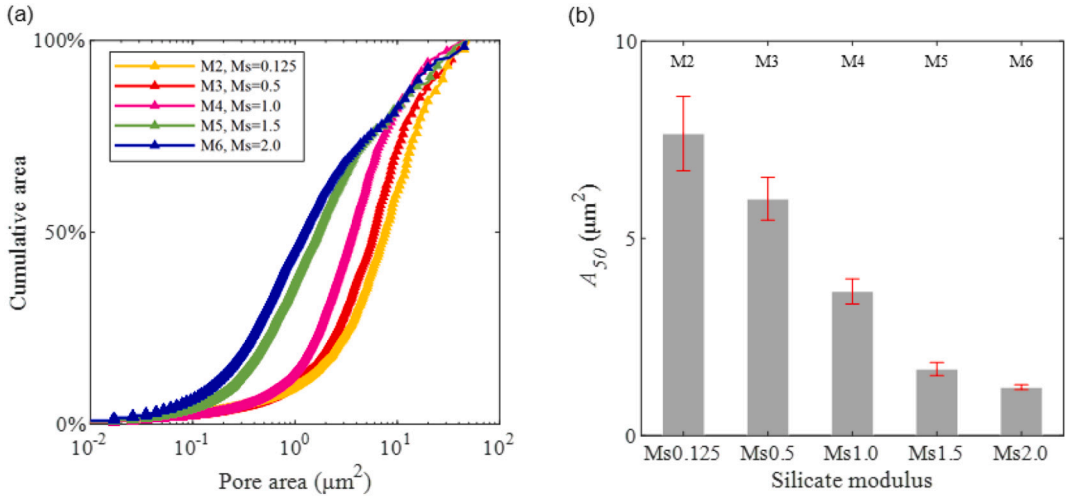

Fig. 12. Pore size properties of water droplets derived from cryo-SEM images of M2, M3, M4, M5, and M6 at 5 min. (a) Pore size distribution curves; (b) A_{50} values.

3.2.3. *Effect of w/b*

The effect of water content was studied by increasing w/b up to 0.45 and 0.5 (M3, M7, and M8), and the microstructures of fresh AAS pastes at 5 min are given in Fig. 13. Obvious changes were detected on the microstructures of pastes with high w/b. As presented in Fig. 13(b), the pore size of water droplets increased with the extra water content, while the thickness of inner walls between droplets was also reduced. In the meantime, more openings could be observed on the inner walls, which indicates that the connectivity of the adjacent water droplets was improved so that water could more easily flow from one pore to another. As the w/b further increased to 0.5 (Fig. 13(c)), microstructural features of the network structure became much less significant, and the water phase became more predominant within the solvent phase. Some big pores were merged, and the inner walls between droplets disappeared. This observation is also evident in the pore size distribution curves and A_{50} values shown in Fig. 14. It can be seen that there is an increase in the size of water droplets with increasing w/b.

All rheological parameters significantly decreased as the w/b increased, as shown in Table 3. The reduction in yield stress and viscosity can be attributed to the extra water content, which resulted in more dispersing effect between slag particles. Meanwhile, the microstructures also suggested the free water became less trapped in the network structure as w/b increased, and thus the collision and interaction between silicate gel and water droplets within the emulsion phase were mitigated. Consequently, the viscosity of fresh AAS paste was modified, which is ascribed not only to the reduction in solid concentration, but also to a reduction in viscosity of the pore solution.

3.2.4. *Aging effect*

The microstructure evolution of Ms0.5 AAS pastes was observed by cryo-SEM at 5, 20, and 60 min, respectively. The mixtures for tests on the aging effect were prepared separately to ensure a comparable shear history. Due to the rapid structural build-up and high stiffness under the cryogenic state of the rest AAS pastes, the microstructural evolution was only studied on M3. As presented in Fig. 15, the interparticle network structure progressively became denser as time elapsed, which is attributed to the precipitation and accumulation of reaction products on the network structure. The pore size distribution curves and A_{50} values are given in Fig. 16. The results show that the average pore size decreased as the pores were gradually filled by the gel-like primary reaction products [27,62,85].

It's been proposed that the structuration of silicate-based AAS can be attributed to the accumulation and hardening of interstitial gels [28]. As the reaction progress, the existing pore structures are more filled and the inner wall between adjacent droplets became thicker (comparing Fig. 15 (c) to (a)). Moreover, the silicate gel in the pore solution became thicker and more viscous due to the accumulation of primary reaction products. In this way, the droplets are more trapped within the pores and difficult to flow and approach each other [86], resulting in the stiffening of the network and structural build-up of the AAS paste.

3.3. *Rheology optimization of AAS*

Similar to the PC materials, AAS made of hydroxide-based activators exhibited a typical suspension microstructure. Reaction products precipitate and accumulate on the slag particles as the activation reaction proceeded. Due to the agglomeration of slag particles (as shown in Fig. 9

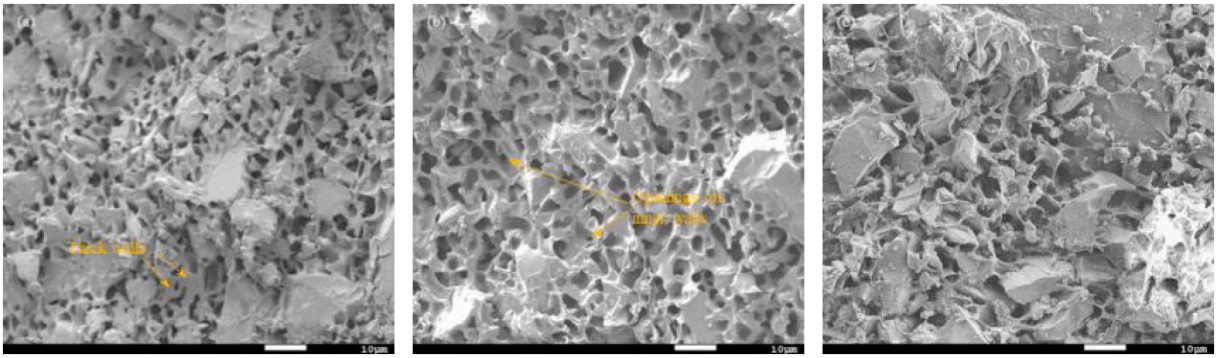

Fig. 13. Microstructure of fresh paste by cryo-SEM (1000×magnification) at 5 min (a) M3, w/b = 0.4; (b) M7, w/b = 0.45; (c) M8, w/b = 0.5.

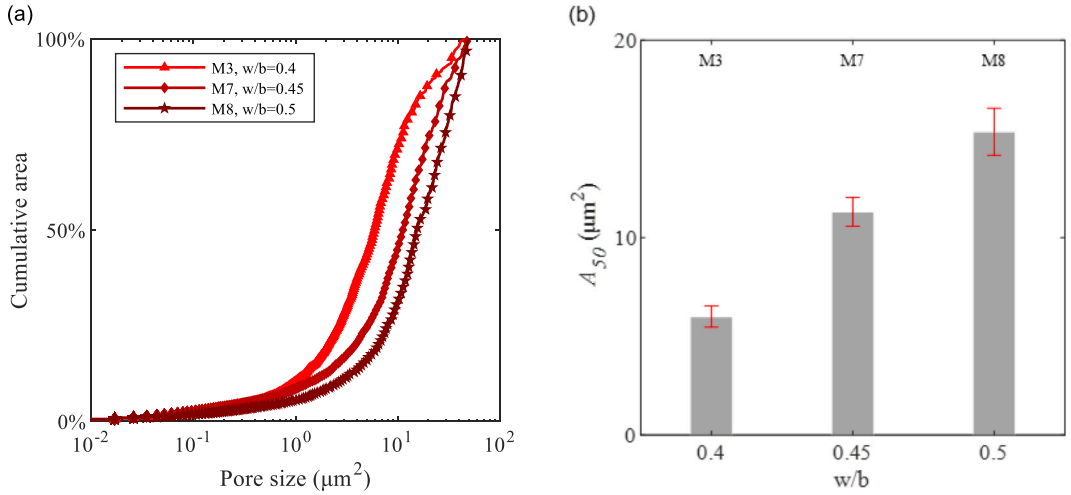

Fig. 14. Pore size properties of water droplets derived from cryo-SEM images of M3, M7 and M8 at 5 min. (a) Pore size distribution curves; (b) A_{50} values.

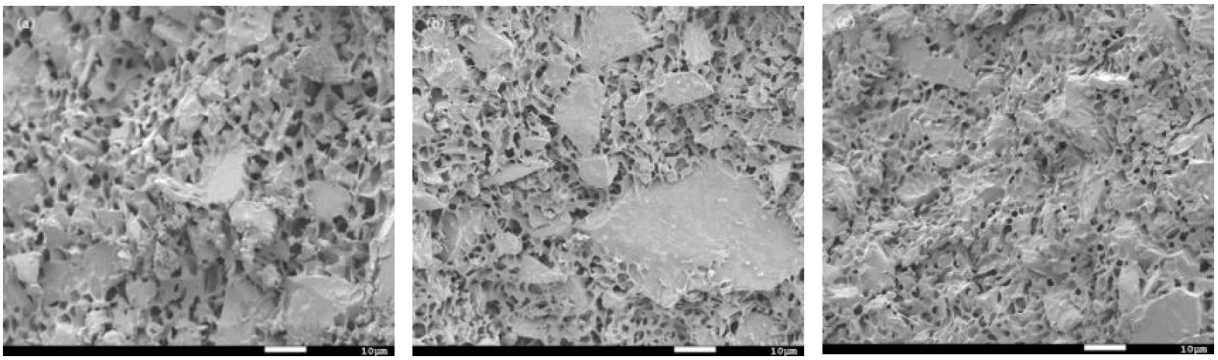

Fig. 15. Microstructure of M3 by cryo-SEM (1000×magnification) (a) 5 min; (b) 20 min; (c) 60 min.

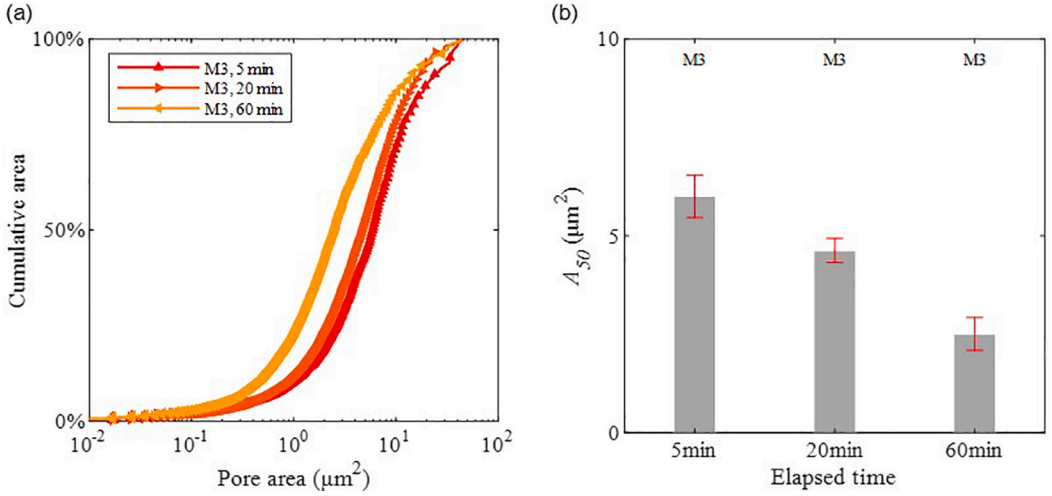

Fig. 16. Pore size properties of droplets derived from cryo-SEM images of M3 at 5, 20, and 60 min (a) Pore size distribution curves; (b) A_{50} values.

(b)), the free water is trapped within the flocs, gradually reducing its fluidity [87]. In this case, the electrostatic repulsion and steric hindrance mechanisms of conventional superplasticizers are still effective. Slag particles could be well dispersed as long as the functional groups of superplasticizer polymers remain undestroyed in the high-alkalinity activators. It's also been confirmed in previous studies that PNS types of superplasticizers are still effective in hydroxide-based AAS mixtures [88,89].

Significant changes were observed by applying silicate species in the activators, a porous network structure has been identified in the AAS paste made of silicate-based activators. The presence of the network structure dispersed the solid slag particles to reduce their direct contact, and the yield stress of AAS mixtures significantly decreased. On the other hand, fine droplets occurred as higher silicate content was applied,

which increased the viscosity of the solvent emulsion phase. Moreover, it's also possible to improve the workability of AAS mixtures by using high w/b, however, the reduction in mechanical properties should be aware that high water content would result in a more porous structure. Accordingly, it's feasible to optimize the rheology of AAM by improving silicate and water content, however, both methods should be limited to a reasonable range to avoid rapid setting and too much reduction in strength, respectively. Regarding the rapid setting in high Ms. AAS mixtures, multiple methods have been proposed to prolong the setting time and improve the fresh properties, such as using a longer mixing time [85,90,91], replacing silicate activator with other alkaline compounds [92,93], and adding admixtures to slow down the activation process (for instance, phosphoric salts and borax) [12,94–96]. Nevertheless, no existing superplasticizer was found to be very effective in silicate media, a fluidizing admixture for silicate-based AAS mixtures is still absent up to date. The microstructural features observed in this study suggest that the working mechanisms for PC superplasticizers might not be applicable in silicate-based AAS mixtures [46,74]. Surfactant could be applied to improve the rheology of the emulsion phase itself, while more understandings on the interactions in the solid-emulsion dispersion are required to better control the rheology of silicate-based AAS mixtures.

4. Conclusions

This study attempts to interpret the early-stage rheological behavior of alkali-activated slag (AAS) paste from microstructural features. The effects of activators, silicate modulus (Ms), and water to binder ratio (w/b) were studied along the activation process. Cryogenic scanning electron microscopy (cryo-SEM) and rheological tests were performed to characterize the evolution of microstructure and rheology of AAS pastes, respectively.

As indicated by the storage modulus evolution, the very early age structural build-up in AAS mixtures was gradually slowed down with an increase in Ms., resulting in an initial dormant period in high Ms. mixtures. However, rapid structuration has been detected in both low and high Ms. mixtures in the first 30 min. The most moderate structural build-up was observed in the Ms0.5 mixture, which can be correlated to the accumulation of intermediate reaction products and thickening of interstitial gels according to the cryo-SEM observations.

In hydroxide-based AAS mixtures, amorphous reaction products have been observed at very early ages which precipitated on the slag surface. The slag particles were attached and bridged to each other through the reaction products to form agglomerations in AAS mixtures, and the free water was trapped in flocs. Thereby, high yield stress has been detected in hydroxide-based AAS mixtures. With the addition of silicate in the activator, a network structure wrapped around the slag particles was identified by cryo-SEM images. Meanwhile, the pore solution showed typical emulsion characteristics, where water droplets are dispersed in the silicate gels. The yield stress of silicate-based AAS paste was significantly reduced as compared to the hydroxide-based mixture as slag particles were dispersed by the silicate gels. However, this effect turned less obvious with further increasing Ms. since slag particles became far apart enough from each other. In silicate-based AAS pastes, the viscosity of the mixtures first increased and later kept nearly constant with increasing Ms. A porous fine emulsion was visualized in high Ms. mixtures, which reveals the highly-viscous nature of the activator as well as the pore solution. Eventually, the rheological parameters of AAS mixtures dramatically reduced with increasing w/b, since the extra water content not only decreased the solid concentration but also improved the connectivity between adjacent water droplets within the emulsion phase.

CRediT authorship contribution statement

Yubo Sun: Conceptualization; Methodology; Investigation; Writing - original draft.

Shizhe Zhang: Methodology; Writing – review & editing.

A. V. Rahul: Conceptualization; Methodology; Writing – original draft.

Yaxin Tao: Methodology; Writing – original draft.

Filip Van Bockstaele: Methodology; Writing – review & editing.

Koen Dewettinck: Writing – review & editing.

Guang Ye: Supervision; Writing – review & editing.

Geert De Schutter: Funding acquisition; Supervision; Writing – review & editing.

Declaration of competing interest

The authors declared that we have no conflicts of interest to this work. We declare that we do not have any commercial or associative interest that represents a conflict of interest in connection with the work submitted.

Acknowledgments

Hercules foundation is acknowledged for its financial support in the acquisition of the scanning electron microscope JEOL JSM-7100F equipped with the cryo-transfer system Quorum PP3010T (grant no. AUGE-09-029) used in this research. The authors wish to thank Mr. Benny Lewille (Ghent University) for helping with the cryo-SEM visualization. This paper presents the research results from the DuRSAAM project. The financial support from the European Union's Horizon 2020 research and innovation programme (ETN DuRSAAM – H2020-MSCA-ITN-2018-813596) is gratefully acknowledged.

References

[1] D.N. Huntzinger, T.D. Eatmon, A life-cycle assessment of Portland cement manufacturing: comparing the traditional process with alternative technologies, J. Clean. Prod. 17 (2009) 668–675.
[2] K.P. Mehta, Reducing the environmental impact of concrete, Concr. Int. 23 (2001) 61–66.
[3] C. Chen, G. Habert, Y. Bouzidi, A. Jullien, Environmental impact of cement production: detail of the different processes and cement plant variability evaluation, J. Clean. Prod. 18 (2010) 478–485.
[4] P. Duxson, D.G. Brice, in: Chemical Research and Climate Change as Drivers in the Commercial Adoption of Alkali Activated Materials, 2010, pp. 145–155, https://doi.org/10.1007/s12649-010-9015-9.
[5] C. Shi, A.F. Jiménez, A. Palomo, Cement and concrete research new cements for the 21st century : the pursuit of an alternative to Portland cement, Cem. Concr. Res. 41 (2011) 750–763, https://doi.org/10.1016/j.cemconres.2011.03.016.
[6] P. Duxson, J.L. Provis, G.C. Lukey, J.S.J.Van Deventer, in: The Role of Inorganic Polymer Technology in the Development of 'Green Concrete,' 37, 2007, pp. 1590–1597, https://doi.org/10.1016/j.cemconres.2007.08.018.
[7] A. Fernández-Jiménez, J.G. Palomo, F. Puertas, Alkali-activated slag mortars: mechanical strength behaviour, Cem. Concr. Res. 29 (1999) 1313–1321, https://doi.org/10.1016/S0008-8846(99)00154-4.
[8] M. Albitar, M.S.M. Ali, P. Visintin, M. Drechsler, Durability evaluation of geopolymer and conventional concretes, Constr. Build. Mater. 136 (2017) 374–385, https://doi.org/10.1016/j.conbuildmat.2017.01.056.
[9] T.A. Aiken, W. Sha, J. Kwasny, M.N. Soutsos, Cement and concrete research resistance of geopolymer and Portland cement based systems to silage ef fl uent attack, Cem. Concr. Res. 92 (2017) 56–65, https://doi.org/10.1016/j.cemconres.2016.11.015.
[10] M. Palacios, P.F.G. Banfill, F. Puertas, Rheology and setting of alkali-activated slag pastes and mortars: effect if organic admixture, ACI Mater. J. 105 (2008) 140–148, https://doi.org/10.14359/19754.
[11] C. Qing-Hua, S.L. Sarkar, A study of rheological and mechanical properties of mixed alkali activated slag pastes, Adv. Cem. Based Mater. 1 (1994) 178–184, https://doi.org/10.1016/1065-7355(94)90009-4.
[12] J.-J. Chang, A study on the setting characteristics of sodium silicate-activated slag pastes, Cem. Concr. Res. 33 (2003) 1005–1011.
[13] C. Lu, Z. Zhang, C. Shi, N. Li, D. Jiao, Q. Yuan, Rheology of alkali-activated materials: a review, Cem. Concr. Compos. 121 (2021), 104061, https://doi.org/10.1016/j.cemconcomp.2021.104061.
[14] E. Deir, B.S. Gebregziabiher, S. Peethamparan, Influence of starting material on the early age hydration kinetics, microstructure and composition of binding gel in alkali activated binder systems, Cem. Concr. Compos. 48 (2014) 108–117, https://doi.org/10.1016/j.cemconcomp.2013.11.010.

[15] S. Song, H.M. Jennings, Pore solution chemistry of alkali-activated ground granulated blast-furnace slag, Cem. Concr. Res. 29 (1999) 159–170, https://doi.org/10.1016/S0008-8846(98)00212-9.
[16] T. Yang, H. Zhu, Z. Zhang, X. Gao, C. Zhang, Q. Wu, Effect of fly ash microsphere on the rheology and microstructure of alkali-activated fly ash/slag pastes, Cem. Concr. Res. 109 (2018) 198–207, https://doi.org/10.1016/j.cemconres.2018.04.008.
[17] X. Dai, S. Aydın, M. Yücel, K. Lesage, G. De Schutter, Cement and concrete research effects of activator properties and GGBFS / FA ratio on the structural build-up and rheology of AAC, Cem. Concr. Res. 138 (2020), 106253, https://doi.org/10.1016/j.cemconres.2020.106253.
[18] K. Vance, A. Dakhane, G. Sant, N. Neithalath, Observations on the rheological response of alkali activated fly ash suspensions: the role of activator type and concentration, Rheol. Acta 53 (2014) 843–855, https://doi.org/10.1007/s00397-014-0793-z.
[19] M.M. Alonso, S. Gismera, M.T. Blanco, M. Lanzón, F. Puertas, Alkali-activated mortars: workability and rheological behaviour, Constr. Build. Mater. 145 (2017) 576–587, https://doi.org/10.1016/j.conbuildmat.2017.04.020.
[20] W. Pan, B. Caswell, G.E. Karniadakis, Rheology, microstructure and migration in brownian colloidal suspensions, Langmuir 26 (2010) 133–142.
[21] M. Fylak, H. Pöllmann, R. Wenda, Application of cryo scanning electron microscopy for the investigation of early OPC-hydration, in: 34th Int. Conf. Cem. Microsc. 2012, 2012, pp. 116–137.
[22] W. Sun, Y. Zhang, W. Lin, Z. Liu, In situ monitoring of the hydration process of K-PS geopolymer cement with ESEM, Cem. Concr. Res. 34 (2004) 935–940.
[23] C. Negro, L.M. Sánchez, E. Fuente, Á. Blanco, J. Tijero, Polyacrylamide induced flocculation of a cement suspension, Chem. Eng. Sci. 61 (2006) 2522–2532.
[24] J.H. Kim, H.J. Yim, R.D. Ferron, In situ measurement of the rheological properties and agglomeration on cementitious pastes, J. Rheol. (N. Y. N. Y) 60 (2016) 695–704.
[25] R.D. Ferron, S. Shah, E. Fuente, C. Negro, Aggregation and breakage kinetics of fresh cement paste, Cem. Concr. Res. 50 (2013) 1–10.
[26] D.-W. Zhang, K.-F. Zhao, H. Li, D. Wang, L. Wang, G. Zhang, Dispersion properties of fly ash–slag powders under the different environment, Constr. Build. Mater. 296 (2021), 123649.
[27] M. Palacios, S. Gismera, M.M. Alonso, J.B. Espinose, D. Lacaillerie, B. Lothenbach, A. Favier, C. Brumaud, F. Puertas, Cement and concrete research early reactivity of sodium silicate-activated slag pastes and its impact on rheological properties, Cem. Concr. Res. 140 (2021), 106302, https://doi.org/10.1016/j.cemconres.2020.106302.
[28] X. Chen, A. Meawad, L.J. Struble, in: Method to Stop Geopolymer Reaction 3275, 2014, pp. 3270–3275, https://doi.org/10.1111/jace.13071.
[29] J.E. Oh, P.J.M. Monteiro, S.S. Jun, S. Choi, S.M. Clark, The evolution of strength and crystalline phases for alkali-activated ground blast furnace slag and fly ash-based geopolymers, Cem. Concr. Res. 40 (2010) 189–196, https://doi.org/10.1016/j.cemconres.2009.10.010.
[30] P. Chindaprasirt, P. De Silva, K. Sagoe-Crentsil, S. Hanjitsuwan, Effect of SiO 2 and Al 2O 3on the setting and hardening of high calcium fly ash-based geopolymer systems, J. Mater. Sci. 47 (2012) 4876–4883, https://doi.org/10.1007/s10853-012-6353-y.
[31] A. Zingg, L. Holzer, A. Kaech, F. Winnefeld, J. Pakusch, S. Becker, L. Gauckler, The microstructure of dispersed and non-dispersed fresh cement pastes - new insight by cryo-microscopy, Cem. Concr. Res. 38 (2008) 522–529, https://doi.org/10.1016/j.cemconres.2007.11.007.
[32] T. Hellemans, G. Abera, I. De Leyn, P. Van der Meeren, K. Dewettinck, M. Eeckhout, B. De Meulenaer, F. Van Bockstaele, Composition, granular structure, and pasting properties of native starch extracted from Plectranthus edulis (Oromo dinich) tubers, J. Food Sci. 82 (2017) 2794–2804, https://doi.org/10.1111/1750-3841.13971.
[33] N. Roos, A.J. Morgan, Cryopreparation of Thin Biological Specimens for Electron Microscopy, Oxford University Press, 1990.
[34] P. Walther, M. Müller, Biological ultrastructure as revealed by high resolution cryo-SEM of block faces after cryo-sectioning, J. Microsc. 196 (1999) 279–287.
[35] N.R. Cameron, D.C. Sherrington, L. Albiston, D.P. Gregory, Study of the formation of the open-cellular morphology of poly (styrene/divinylbenzene) polyHIPE materials by cryo-SEM, Colloid Polym. Sci. 274 (1996) 592–595.
[36] G. Desbois, J.L. Urai, P.A. Kukla, Morphology of the pore space in claystones–evidence from BIB/FIB ion beam sectioning and cryo-SEM observations, EEarth Discuss. 4 (2009) 1–19.
[37] M. Fylak, J. Göske, W. Kachler, R. Wenda, H. Pöllmann, Cryotransfer scanning electron microscopy for the study of cementitious systems, Microsc. Anal. 102 (2006) 9–12.
[38] J. Lepault, J. Dubochet, Freezing, fracturing, and etching artifacts in particulate suspensions, J. Ultrastruct. Res. 72 (1980) 223–233.
[39] J. Dubochet, J.-J. Chang, R. Freeman, J. Lepault, A.W. McDowall, Frozen aqueous suspensions, Ultramicroscopy 10 (1982) 55–61.
[40] A.K. Pathan, J. Bond, R.E. Gaskin, Sample preparation for SEM of plant surfaces, Mater. Today 12 (2010) 32–43.
[41] R. Talevi, V. Barbato, I. Fiorentino, S. Braun, C. De Stefano, R. Ferraro, S. Sudhakaran, R. Gualtieri, Successful slush nitrogen vitrification of human ovarian tissue, Fertil. Steril. 105 (2016) 1523–1531.
[42] S. Yavin, A. Aroyo, Z. Roth, A. Arav, Embryo cryopreservation in the presence of low concentration of vitrification solution with sealed pulled straws in liquid nitrogen slush, Hum. Reprod. 24 (2009) 797–804.
[43] T.K. Yoon, D.R. Lee, S.K. Cha, H.M. Chung, W.S. Lee, K.Y. Cha, Survival rate of human oocytes and pregnancy outcome after vitrification using slush nitrogen in assisted reproductive technologies, Fertil. Steril. 88 (2007) 952–956.
[44] P. Krivenko, R. Drochytka, A. Gelevera, E. Kavalerova, Mechanism of preventing the alkali–aggregate reaction in alkali activated cement concretes, Cem. Concr. Compos. 45 (2014) 157–165.
[45] S. Zhang, Z. Li, B. Ghiassi, S. Yin, G. Ye, Fracture properties and microstructure formation of hardened alkali-activated slag/fly ash pastes, Cem. Concr. Res. 144 (2021), 106447.
[46] M.F. Alnahhal, T. Kim, A. Hajimohammadi, Distinctive rheological and temporal viscoelastic behaviour of alkali-activated fly ash/slag pastes: a comparative study with cement paste, Cem. Concr. Res. 144 (2021), 106441, https://doi.org/10.1016/j.cemconres.2021.106441.
[47] Q. Yuan, D. Zhou, K.H. Khayat, D. Feys, C. Shi, On the measurement of evolution of structural build-up of cement paste with time by static yield stress test vs. Small amplitude oscillatory shear test, Cem. Concr. Res. 99 (2017) 183–189.
[48] D. Jiao, K. El Cheikh, C. Shi, K. Lesage, G. De Schutter, Structural build-up of cementitious paste with nano-Fe3O4 under time-varying magnetic fields, Cem. Concr. Res. 124 (2019), 105857.
[49] Q. Yuan, X. Lu, K.H. Khayat, D. Feys, C. Shi, Small amplitude oscillatory shear technique to evaluate structural build-up of cement paste, Mater. Struct. 50 (2017) 1–12.
[50] A. Favier, G. Habert, J.B. D'Espinose De Lacaillerie, N. Roussel, Mechanical properties and compositional heterogeneities of fresh geopolymer pastes, Cem. Concr. Res. 48 (2013) 9–16, https://doi.org/10.1016/j.cemconres.2013.02.001.
[51] A. Poulesquen, F. Frizon, D. Lambertin, Rheological behavior of alkali-activated metakaolin during geopolymerization, J. Non-Cryst. Solids 357 (2011) 3565–3571, https://doi.org/10.1016/j.jnoncrysol.2011.07.013.
[52] M. Chen, L. Yang, Y. Zheng, Y. Huang, L. Li, P. Zhao, S. Wang, L. Lu, X. Cheng, Yield stress and thixotropy control of 3D-printed calcium sulfoaluminate cement composites with metakaolin related to structural build-up, Constr. Build. Mater. 252 (2020), 119090.
[53] H. Yao, Z. Xie, Z. Li, C. Huang, Q. Yuan, X. Zheng, The relationship between the rheological behavior and interlayer bonding properties of 3D printing cementitious materials with the addition of attapulgite, Constr. Build. Mater. 316 (2022), 125809.
[54] I. González-Taboada, B. González-Fonteboa, F. Martínez-Abella, S. Seara-Paz, Thixotropy and interlayer bond strength of self-compacting recycled concrete, Constr. Build. Mater. 161 (2018) 479–488.
[55] A.I. Laskar, R. Bhattacharjee, Rheology of Fly-ash-based geopolymer concrete, ACI Mater. J. 108 (2011).
[56] C. Kyomugasho, S. Christiaens, D. Van de Walle, A.M. Van Loey, K. Dewettinck, M. E. Hendrickx, Evaluation of cation-facilitated pectin-gel properties: cryo-SEM visualisation and rheological properties, Food Hydrocoll. 61 (2016) 172–182.
[57] E.T. Arena, C.T. Rueden, M.C. Hiner, S. Wang, M. Yuan, K.W. Eliceiri, Quantitating the cell: turning images into numbers with ImageJ, Wiley Interdiscip. Rev. Dev. Biol. 6 (2017), https://doi.org/10.1002/wdev.260.
[58] G. Beersaerts, A. Vananroye, D. Sakellariou, C. Clasen, Y. Pontikes, Rheology of an alkali-activated fe-rich slag suspension: identifying the impact of the activator chemistry and slag particle interactions, J. Non-Cryst. Solids 561 (2021), 120747.
[59] P. Duxson, A. Fernández-Jiménez, J.L. Provis, G.C. Lukey, A. Palomo, J.S.J. Van Deventer, Geopolymer technology: the current state of the art, J. Mater. Sci. 42 (2007) 2917–2933, https://doi.org/10.1007/s10853-006-0637-z.
[60] Y. Zuo, G. Ye, Preliminary interpretation of the induction period in hydration of sodium hydroxide/silicate activated slag, Materials (Basel) 13 (2020) 1–19, https://doi.org/10.3390/ma13214796.
[61] N. Roussel, G. Ovarlez, S. Garrault, C. Brumaud, The origins of thixotropy of fresh cement pastes, Cem. Concr. Res. 42 (2012) 148–157, https://doi.org/10.1016/j.cemconres.2011.09.004.
[62] B.S. Gebregziabiher, R. Thomas, S. Peethamparan, Very early-age reaction kinetics and microstructural development in alkali-activated slag, Cem. Concr. Compos. 55 (2015) 91–102, https://doi.org/10.1016/j.cemconcomp.2014.09.001.
[63] B.S. Gebregziabiher, R.J. Thomas, S. Peethamparan, Temperature and activator effect on early-age reaction kinetics of alkali-activated slag binders, Constr. Build. Mater. 113 (2016) 783–793, https://doi.org/10.1016/j.conbuildmat.2016.03.098.
[64] C. Shi, R.L. Day, A calorimetric study of early hydration of alkali-slag cements, Cem. Concr. Res. 25 (1995) 1333–1346.
[65] P. Duxson, J.L. Provis, Designing precursors for geopolymer cements, J. Am. Ceram. Soc. 91 (2008) 3864–3869, https://doi.org/10.1111/j.1551-2916.2008.02787.x.
[66] R. Cao, S. Zhang, N. Banthia, Y. Zhang, Z. Zhang, Interpreting the early-age reaction process of alkali-activated slag by using combined embedded ultrasonic measurement, thermal analysis, XRD, FTIR and SEM, Compos. Part B Eng. 186 (2020), 107840, https://doi.org/10.1016/j.compositesb.2020.107840.
[67] Z. Huanhai, W. Xuequan, X. Zhongzi, T. Mingshu, Kinetic study on hydration of alkali-activated slag, Cem. Concr. Res. 23 (1993) 1253–1258.
[68] A.M. Mostafa, A. Yahia, New approach to assess build-up of cement-based suspensions, Cem. Concr. Res. 85 (2016) 174–182.
[69] A. Poulesquen, F. Frizon, D. Lambertin, Rheological behavior of alkali-activated metakaolin during geopolymerization, J. Non-Cryst. Solids 357 (2011) 3565–3571, https://doi.org/10.1016/j.jnoncrysol.2011.07.013.
[70] J. Rouyer, A. Poulesquen, Evidence of a fractal percolating network during geopolymerization, J. Am. Ceram. Soc. 98 (2015) 1580–1587.
[71] J. Davidovits, Properties of geopolymer cements, in: First Int. Conf. Alkaline Cem. Concr, Kiev State Technical University Kiev, Ukraine, 1994, pp. 131–149.

[72] H.H.C. Wong, A.K.H. Kwan, Rheology of cement paste: role of excess water to solid surface area ratio, J. Mater. Civ. Eng. 20 (2008) 189–197, https://doi.org/10.1061/(asce)0899-1561(2008)20:2(189).
[73] M.H. Hubler, J.J. Thomas, H.M. Jennings, Influence of nucleation seeding on the hydration kinetics and compressive strength of alkali activated slag paste, Cem. Concr. Res. 41 (2011) 842–846, https://doi.org/10.1016/j.cemconres.2011.04.002.
[74] A. Favier, J. Hot, G. Habert, N. Roussel, J.B. D'Espinose De Lacaillerie, Flow properties of MK-based geopolymer pastes. A comparative study with standard Portland cement pastes, Soft Matter 10 (2014) 1134–1141, https://doi.org/10.1039/c3sm51889b.
[75] A. Kashani, J.L. Provis, G.G. Qiao, J.S.J. Van Deventer, The interrelationship between surface chemistry and rheology in alkali activated slag paste, Constr. Build. Mater. 65 (2014) 583–591, https://doi.org/10.1016/j.conbuildmat.2014.04.127.
[76] N. Roussel, A. Lemaître, R.J. Flatt, P. Coussot, Steady state flow of cement suspensions: a micromechanical state of the art, Cem. Concr. Res. 40 (2010) 77–84, https://doi.org/10.1016/j.cemconres.2009.08.026.
[77] B.C. Tatar, G. Sumnu, S. Sahin, Rheology of Emulsions, Elsevier Ltd, 2017, https://doi.org/10.1016/B978-0-08-100431-9.00017-6.
[78] T.G. Mason, in: New Fundamental Concepts in Emulsion Rheology 4, 1999, pp. 231–238.
[79] K. Vance, A. Kumar, G. Sant, N. Neithalath, The rheological properties of ternary binders containing Portland cement, limestone, and metakaolin or fly ash, Cem. Concr. Res. 52 (2013) 196–207.
[80] I.M. Krieger, T.J. Dougherty, A mechanism for non-newtonian flow in suspensions of rigid spheres, Trans. Soc. Rheol. 3 (1959) 137–152.
[81] L. Struble, G.-K. Sun, Viscosity of Portland cement paste as a function of concentration, Adv. Cem. Based Mater. 2 (1995) 62–69.
[82] R. Pal, Effect of droplet size on the rheology of emulsions, AIChE J. 42 (1996) 3181–3190.
[83] R. Chanamai, D.J. McClements, Dependence of creaming and rheology of monodisperse oil-in-water emulsions on droplet size and concentration, Colloids Surf. A Physicochem. Eng. Asp. 172 (2000) 79–86.
[84] H. Jansson, D. Bernin, K. Ramser, Silicate Species of Water Glass and Insights for Alkali-activated Green Cement 067167, 2017, https://doi.org/10.1063/1.4923371.
[85] F. Puertas, C. Varga, M.M. Alonso, Rheology of alkali-activated slag pastes. Effect of the nature and concentration of the activating solution, Cem. Concr. Compos. 53 (2014) 279–288, https://doi.org/10.1016/j.cemconcomp.2014.07.012.
[86] N. Sun, H. Jiang, X. Wang, K. Jin, Research on factors affecting heavy oil-in-water emulsion rheology and pressure drop, J. Dispers. Sci. Technol. 39 (2018) 411–422, https://doi.org/10.1080/01932691.2017.1324795.
[87] M. Yang, H.M. Jennings, Influences of mixing methods on the microstructure and rheological behavior of cement paste, Adv. Cem. Based Mater. 2 (1995) 70–78.
[88] M. Palacios, Y.F. Houst, P. Bowen, F. Puertas, Adsorption of superplasticizer admixtures on alkali-activated slag pastes, Cem. Concr. Res. 39 (2009) 670–677, https://doi.org/10.1016/j.cemconres.2009.05.005.
[89] M. Palacios, F. Puertas, Effect of superplasticizer and shrinkage-reducing admixtures on alkali-activated slag pastes and mortars, Cem. Concr. Res. 35 (2005) 1358–1367, https://doi.org/10.1016/j.cemconres.2004.10.014.
[90] M. Palacios, F. Puertas, Effectiveness of mixing time on hardened properties of waterglass-activated slag pastes and mortars, ACI Mater. J. 108 (2011) 73.
[91] F. Puertas, B. González-Fonteboa, I. González-Taboada, M.M. Alonso, M. Torres-Carrasco, G. Rojo, F. Martínez-Abella, Alkali-activated slag concrete: fresh and hardened behaviour, Cem. Concr. Compos. (2018), https://doi.org/10.1016/j.cemconcomp.2017.10.003.
[92] S. Uppalapati, L. Vandewalle, Ö. Cizer, Monitoring the setting process of alkali-activated slag-fly ash cements with ultrasonic P-wave velocity, Constr. Build. Mater. 271 (2021), 121592.
[93] Z. Jiao, Y. Wang, W. Zheng, W. Huang, Effect of dosage of sodium carbonate on the strength and drying shrinkage of sodium hydroxide based alkali-activated slag paste, Constr. Build. Mater. 179 (2018) 11–24.
[94] C. Gong, N. Yang, Effect of phosphate on the hydration of alkali-activated red mud–slag cementitious material, Cem. Concr. Res. 30 (2000) 1013–1016.
[95] S.W. Wijaya, J. Satria, A. Sugiarto, D. Hardjito, The use of borax in deterring flash setting of high calcium fly ash based geopolymer, in: Mater. Sci. Forum, Trans Tech Publ, 2016, pp. 416–420.
[96] S.Y. Oderji, B. Chen, C. Shakya, M.R. Ahmad, S.F.A. Shah, Influence of superplasticizers and retarders on the workability and strength of one-part alkali-activated fly ash/slag binders cured at room temperature, Constr. Build. Mater. 229 (2019), 116891, https://doi.org/10.1016/j.conbuildmat.2019.116891.